CrossMark

RESEARCH PAPER

Facile fabrication of Pt–Ni alloy nanoparticles supported on reduced graphene oxide as excellent electrocatalysts for hydrogen evolution reaction in alkaline environment

Zuokai Du · Yilong Wang (iD) **· Junsheng Li · Jinping Liu**

Abstract Development of high-performance electrocatalysts in basic electrolyte is of significance for the decrease in unnecessary energy consumption for production of hydrogen. Herein, we have demonstrated one-step chemical reduction strategy to fabricate platinum–nickel alloy nanoparticle–supported reduced graphene oxide (rGO) as excellent electrocatalysts for hydrogen evolution reaction (HER) in basic condition. Graphene-supported alloy nanocatalysts are achieved by simply controlling the molar ratios of bimetallic precursors. We confirm that nickel species on the surface of as-synthesized nanocatalysts tend to be oxidized as nickel hydroxide during the fabrication. Our nanocatalysts synthesized at the equivalent molar ratios of platinum and nickel salts exhibit much higher electrocatalytic activity for HER than the commercial Pt/C and graphene-supported Pt counterparts in same conditions. The performance improvement is not only attributed to nickel hydroxide layer on our nanocatalysts facilitating the decomposition of water in basic media but also ascribed to the partial replacement of Pt atoms by Ni ones decreasing the Pt–H bond energy and improving desorption of hydrogen atoms on Pt–Ni alloy nanocatalysts. Furthermore, our nanocatalysts present excellent HER catalytic stability. Our results will provide a facile and effective strategy on the development of the excellent Pt-containing composite nanocatalysts for applications in electrocatalysis.

Keywords Pt–Ni alloy nanoparticles · Reduced graphene oxide · Electrocatalysis · Hydrogen evolution reaction

Introduction

Considerable attention has recently been paid to electrocatalysis for HER because it is a promising and effective technique to achieve ecofriendly hydrogen (H_2) production (Liu et al. 2015; Liu et al. 2017; Wu et al. 2018; Xu et al. 2018; Chen et al. 2017; Hao et al. 2018; Zhang et al. 2017a, b; Liu et al. 2018). Enormous efforts have been made in attempt to investigate a variety of advanced electrocatalysts, which will be expected to effectively generate H_2 from water splitting by the electrochemical technology (Zou et al. 2017; Zou et al. 2018; Zhang et al. 2018a). Among these electrocatalysts, Pt-based materials have so far been proven as the most active ones for HER, but high cost makes them difficult for vast industrial usage (Bao et al. 2017). Additionally, alkaline water electrolysis has been regarded as the most likely technology to be industrialized hydrogen production due to its unique advantages including unlimited reactant availability, good manufacturing safety, stable output, and high product

Z. Du · Y. Wang (✉) · J. Li · J. Liu (✉)
School of Chemistry, Chemical Engineering and Life Science, Wuhan University of Technology, 122# Luoshi Road, Wuhan 430070, People's Republic of China
e-mail: wangyilong@whut.edu.cn
e-mail: liujp@whut.edu.cn

purity (Yin et al. 2015). However, the sluggish kinetics of HER in a basic environment leads to unnecessary energy losses, which severely impedes the wide application of Pt-based catalysts (Yin et al. 2015). Obviously, improving the catalytic activity and lowering the cost of these Pt-based catalysts are the major bottlenecks in this field. Therefore, it is urgent to achieve an efficient design approach to the development of the high-performance and cost-effective electrocatalysts for HER in basic solution.

The investigation on Pt-containing bimetallic or trimetallic nanostructures as electrocatalysts may provide an efficient method to address these issues. In this method, platinum can be partially substituted by low-cost 3d-transition metals to design and fabricate the hybrid electrocatalysts. Following this viewpoint, the Pt-based polymetallic catalysts (e.g., platinum–iron, platinum–copper, and platinum–ruthenium–nickel) have been introduced into the cathodic oxygen reduction reaction (ORR) in direct methanol fuel cells (DMFCs) to improve catalytic performance and lower the content of platinum of them as well (He et al. 2007; Chen et al. 2009; Loukrakpam et al. 2011; Yu and Manthiram 2018; Mezzavilla et al. 2016; Wang et al. 2010). In their opinion, the lattice shrink and strain should be responsible for the enhancement in catalytic activities, which is ascribed to the change of Pt–Pt bond length, and the skin effect of platinum after the replacement of platinum by other 3d-transition metals (Loukrakpam et al. 2011). Subsequently, Pt–Ni alloy nanoparticles (NPs) have been developed as excellent catalysts for anodic methanol oxidation reaction (MOR) in DMFCs. This is because Pt–Ni alloy NPs could weaken the adsorption of carbon monoxide on platinum and promote to remove the intermediate CO during catalytic reaction (Hu et al. 2012; Li et al. 2013a). Furthermore, the oxygen evolution reaction (OER), as one of main reactions of electrochemical water splitting (Fang et al. 2018), have been efficiently catalyzed by the Pt–Ir alloy nanocrystals based on manipulating alloying and surface oxidation state of Ir (Zhang et al. 2017a, b). More recently, Lee's and Xia's groups have demonstrated the fabrication of Pt–Ni octahedral nanocrystals with the diameter of about 9 nm, which will be employed as a kind of promising electrocatalysts towards HER (Kavian et al. 2016). Interestingly, this design strategy for HER originated from Pt–Ni nanocrystals which had been employed as the high-performance electrocatalysts for ORR (He et al. 2007). However, in our viewpoint,

the precise role played by the introduction of Ni into Pt should be further investigated to achieve the excellent Pt-containing hybrid nanocatalysts. Moreover, the complicated synthesis limits the practical application of the Pt–Ni octahedra as well.

On the other hand, the supporting materials (SMs) take an important role in determining the average diameter of the metal NPs on them. This greatly influences the catalytic performance and stability of these supported catalysts (Konopka et al. 2011; Zhu et al. 2018). Generally, graphene is considered as the ideal SMs for the metal nanoparticles among many carbon materials, owing to the inertness in harsh chemical or electrochemical conditions, unique 2D materials with high surface area, and unusual electronic properties and low cost (Kou et al. 2011; Zhang et al. 2018b). In particular, its physicochemical properties are accessible to be further improved by the doping of nonmetal elements. For example, nitrogen-doped rGO can demonstrate distinctive physicochemical characteristics because of the introduction of a great number of doping-induced defects (Wang et al. 2014; Liu et al. 2016). According to the previously reported literatures, N doping–induced metal–support interaction between rGO and metal can effectively protect from the agglomeration of metal nanoparticles and obviously enhance the mass transport of reactants to metal NPs (Bao et al. 2017; Pylypenko et al. 2013; Fan et al. 2015).

To our best knowledge, the previously reported Pt–Ni alloy/rGO nanocatalysts have been utilized as the highly efficient catalysts for the reduction of p-nitrophenol (4-NP) into p-aminophenol (4-AP) with NaBH$_4$ (Zhao et al. 2016; Sahoo et al. 2014). In our opinion, their electrocatalysis for HER should be further investigated here. Inspired by these, we have developed a facile design strategy in which we grow bimetallic NPs with a series of Pt–Ni molar ratio on two-dimensional (2D) nitrogen-doped rGO to construct excellent electrocatalysts for HER in basic solution. The influence of the crystal structure on HER electrochemical activity of Pt–Ni alloy NPs decorated on rGO is systematically investigated, especially the positive influence of nickel on platinum. It can be reasonably illustrated as follows: on the one hand, nickel species on the surface of as-synthesized nanocatalysts tend to be oxidized as nickel hydroxide during the fabrication, which is advantageous to promote the decomposition of water in basic condition. On the other hand, alloying of Pt and Ni could decrease the Pt–H bond energy and improve desorption

of hydrogen atoms from electrocatalysts. Therefore, the as-synthesized Pt–Ni/rGO nanocatalysts exhibit the relatively high catalytic activity towards HER to the commercial Pt/C and Pt/rGO samples in same conditions. In addition, such Pt–Ni/rGO nanocatalysts can present magnetic recollection of Ni besides fully utilizing the catalytic abilities of both metals. Last but not least, Ni(OH)$_2$ layer on our nanocatalysts can effectively protect them against corrosion; then, they present excellent HER catalytic stability. Our work will afford a fundamental investigation for the development of the excellent Pt-based hybrid nanocatalysts and promise their important application in catalysis and energy conversion.

Experimental sections

Synthesis of Pt–Ni/rGO nanocatalysts

Graphene oxide (GO) was prepared according to the previously reported literature (Liu et al. 2016), which was described in online Electronic Supplementary Material. The process for synthesis of metal/rGO nanocatalysts was illustrated in the following steps: (1) a certain amount of chloroplatinic acid and nickel chloride was dissolved in 15.00 mL the deionized water; then, this solution was added into 15.00 mL of GO suspension (0.6 mg mL^{-1}, the deionized water as the solvent) under magnetic stirring. (2) Subsequently, 0.1 g polyvinylpyrrolidone (PVP, K30) was added into the mixture mentioned above. After ultrasonication for 30 min, 2.00 mL of hydrazine (85 wt%) and 1.00 mL of ammonium hydroxide (28 wt%) were slowly dropped the mixed system, respectively. The whole reaction system was placed into a Teflon-lined autoclave, which was sealed and treated at 180 °C for 6 h. By adjusting the amount of precursors, the metal/rGO nanocatalysts with Pt^{4+}/Ni^{2+} molar ratios of 1:0, 3:1, 3:2, 1:1, and 0:1 were prepared, respectively. These samples were denoted as Pt/rGO, Pt–Ni(3:1)/rGO, Pt–Ni(3:2)/rGO, Pt–Ni(1:1)/rGO, and Ni/rGO, according to Pt^{4+}/Ni^{2+} molar ratios, hereafter. The weight percentage of total metal of all electrocatalysts was adjusted to about 40% in our experiments. After the reaction was accomplished, the corresponding samples were washed with ethanol for three times, finally dried under vacuum at 25 °C for 2 h. Among these as-obtained samples, Pt–Ni(1:1)/rGO nanocatalysts were called as the typical (Pt–Ni/rGO)

nanocatalysts or the typical samples. Other experimental details on materials, characterization, and electrochemical measurements were described in online Electronic Supplementary Material.

Results and discussion

Characterization of Pt–Ni/rGO nanocatalysts

Figure 1a displays that rGO is ultrathin, wrinkled, and transparent. Figure 1b–d presents the integrated characterization of Pt–Ni(1:1)/rGO nanocatalysts (the typical samples). Transmission electron microscopy (TEM) image of these nanocatalysts (Fig. 1b) indicates that NPs show no apparent aggregation and are distributed uniformly on rGO. These nanoparticles of the typical samples are regarded as spherical ones with the mean diameter of ∼ 20 nm from inset of Fig. 1b. Meanwhile, rGO is indicated by the red arrow in Fig. 1b. Figure 1c displays the energy-dispersive X-ray spectroscopy (EDX) spectrum of the typical samples, indicative of the coexistence of C, O, Ni, Pt, and Cu elements. It can be sure that Ni and Pt elements should come from metal NPs on rGO. Except for Ni and Pt peaks, the presence of C and Cu elements should be attributed to rGO and the substrate of copper grid, respectively. The crystalline structures of the metal/rGO nanocatalysts synthesized at various Pt^{4+}/Ni^{2+} molar ratios are investigated by X-ray diffraction (XRD) measurements (Figs. 1c and 2). From Fig. 2b, characteristic diffraction peaks of Pt/rGO samples at 39.8° and 46.4° are indexed to a face-centered cubic (fcc) phase of platinum, corresponding to the planes of (111) and (200) (JCPDS 04-0802) (Hu et al. 2012). For Ni/rGO samples, two diffraction peaks in Fig. 2e at 2θ of 44.1° (111) and 51.5° (200) match exactly with the standard pattern of fcc nickel (JCPDS 04-0787) as well. However, XRD pattern of the typical samples demonstrates two diffraction peaks at 2θ of 41.3° and 47.8° in Fig. 1d. At the same time, no characteristic peaks of Ni(OH)$_2$ and other crystalline impurity are detected. According to this figure, two diffraction peaks shift to high angles in comparison with those of Pt/rGO samples, suggesting the formation of alloy NPs on rGO. To further reveal the structure of metal NPs on the typical samples, their high-resolution TEM (HRTEM) image is displayed in Fig. 1e. This figure clearly demonstrates the characteristic lattice spacing of an individual nanoparticle of the typical Pt–Ni(1:1)/rGO nanocatalysts.

Specifically, the lattice spacing is observed to 0.219 nm, which corresponds to the {111} facets of Pt–Ni alloy (Li et al. 2013a) and is almost identical to the theoretical value from XRD pattern listed in Table S1. The scanning TEM (STEM)-EDX line-scanning profiles (Fig. 1f) exhibit that two metal elements distribute uniformly and overlap completely throughout the whole nanoparticle. This suggests that these metal NPs on rGO have the homogeneous Pt–Ni alloy rather than heterogeneous or core/shell (Pt/Ni) nanostructure. And the molar percentage of platinum in total metals is calculated to be about 51%, which almost approaches to their theoretical value. Furthermore, the corresponding elemental maps (Fig. 1g, h) display that these metal elements are well dispersed throughout an individual metal nanoparticle. Based on the above evidences, the Pt–Ni alloy NPs supported on rGO which can be employed as the high-performance electrocatalysts for HER are successfully synthesized in this work.

Considering that the structure of the as-synthesized nanocatalysts could be effectively regulated by simply changing the molar ratios of platinum to nickel salts (*F*), the effect of metal/rGO nanocatalysts synthesized at various *F* on their XRD patterns is systematically investigated in Fig. 2. The weak and broad diffraction peak at $2\theta = 24°$ is originated from rGO (Tang et al. 2009) for each sample. Except for curve b and curve e in Fig. 2, the other diffraction peaks of samples synthesized at $F = 3:1$ or 3:2 correspond to neither Pt nor Ni as the typical samples. This further confirms the formation of alloys in our experiments for these samples. Moreover, the diffraction peaks of all samples gradually convert to Ni ones while *F* decreases. Therefore, the as-synthesized samples present smaller *d*-spacing value (*d*) and lattice parameter of platinum than Pt/rGO ones. Both *d* and lattice parameter of the as-synthesized samples decrease with the decrease in the molar percentage of Pt (Table S1). And the composition or atom ratio of the as-synthesized Pt–Ni/rGO samples measured by inductively coupled plasma-atomic emission spectroscopy (ICP-AES) can also be effectively controlled by simply changing *F* listed in Table S1.

Subsequently, we investigate the influence of *F* on the diameter of the alloy nanoparticles for these nanocatalysts. TEM images of the metal/rGO nanocatalysts synthesized at various *F* are shown in Fig. 3. According to this figure, there is no obvious difference in the diameter of these alloy nanoparticles for all samples, and the diameter of these alloy

nanoparticles is almost same as that of the typical samples. It can be explained from the viewpoint of nucleation. The rate of the formation nuclei, $\frac{dN}{dt}$, is written as the following equation,

$$\frac{dN}{dt} = A\exp\left[-\frac{16\pi\gamma^3 V_m^2}{3k_B^3 T^3 N_A^2 (\ln S_n)^2}\right] \tag{1}$$

where N, A, γ, V_m, k_B, T, N_A, and S_n are the number of nuclei, the preexponential factor, the surface energy per unit area of nuclei, the molar volume of the monomer in crystal, the Boltzmann constant, reaction temperature, Avogadro's number, and the level of supersaturation for nucleation, respectively (Kwon and Hyeon 2011; Wang et al. 2017). Specifically, three experimental parameters, such as S_n, T, and γ, can be controlled in the synthesis. In this work, S_n and T should have no significant effect on nucleation. This is because the molar number and T are kept constant. Herein, employing the surfactant, PVP as additives, could decrease γ so as to improve the nucleation rate (Bian et al. 2018; Wang et al. 2015, 2016, 2017). In consequence, nucleation burst leads to the increase in the number of nuclei and the decrease in the diameter of alloy nanoparticles. This opinion can be confirmed by the additional experiment without PVP as surfactant, other conditions as the typical experiments (Fig. S1). In terms of this figure, the diameter of metal nanoparticles on rGO is as high as over 50 nm. Obviously, the diameter of nanoparticles shown in Fig. S1 is much bigger than that of metal nanoparticles in Fig. 3, which is reasonably explained by the assumption that poor nucleation results in the increase in the diameter of metal nanoparticles.

Figures 4 and 5 present X-ray photoelectron spectroscopy (XPS) spectra of the typical samples. The full spectrum (Fig. 4a) shows that the typical samples are composed of O, N, C, Pt, and Ni elements. The high-resolution N 1s spectrum (Fig. 4b) is deconvoluted to three peaks that are attributed to pyridinic N (398.2 eV), pyrrolic N (399.5 eV), and substitutional N (401.0 eV). The peak at 401.0 eV in this figure indicates the successful N doping in the reduction of GO by the one-step hydrothermal approach (Lv et al. 2012). The high-resolution C 1s spectrum (Fig. 4c) is able to be deconvoluted to five main peaks. Among these peaks, the major one at 284.6 eV is ascribed to the sp^2 hybridized carbon (C–C/C=C), suggesting that most of carbon atoms of the typical samples present embedded within honeycomb lattice of rGO (Liu et al. 2016). Other peaks
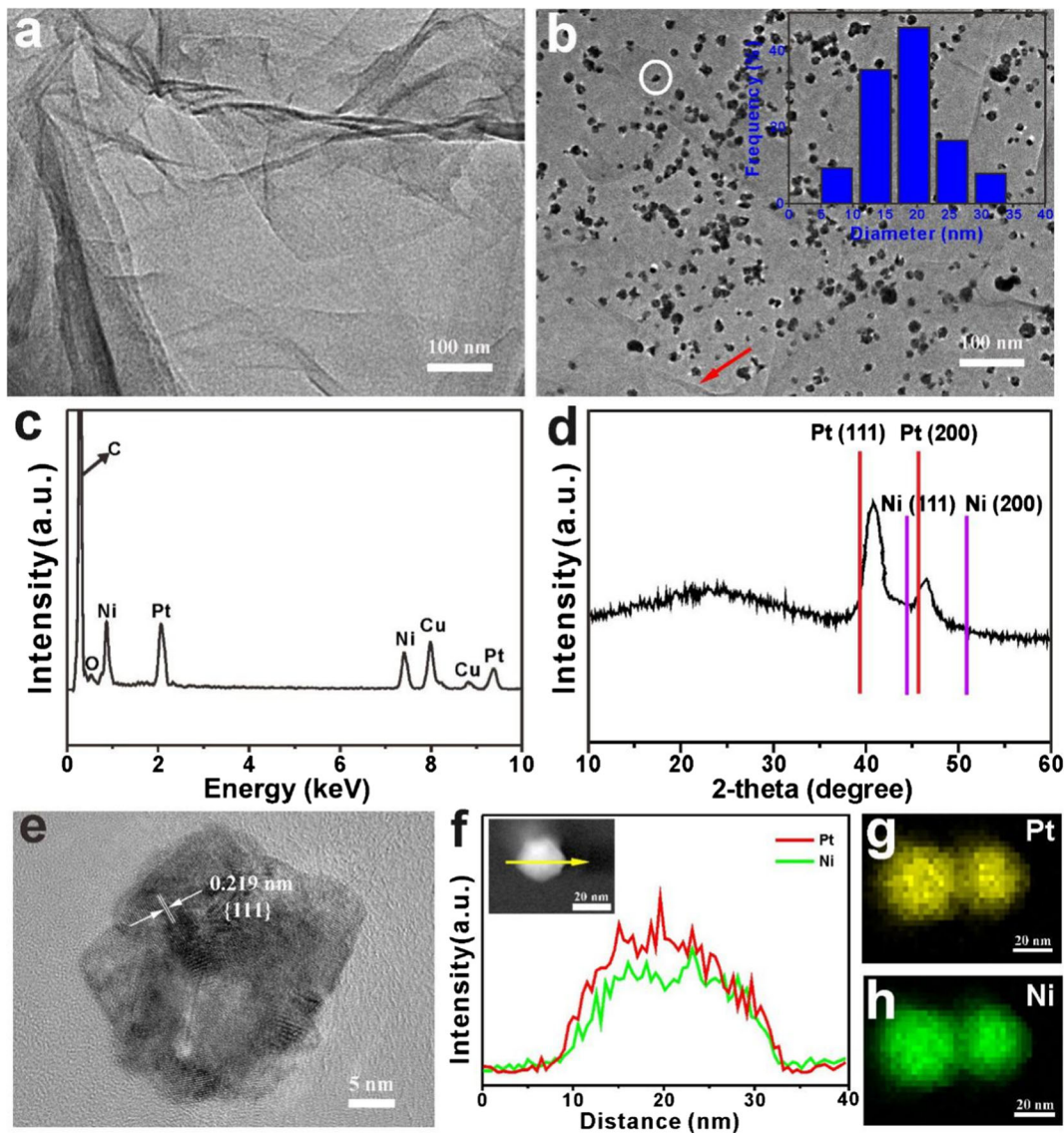
Fig. 1 **a** TEM image of rGO. **b** TEM image, **c** EDX spectrum, and **d** XRD pattern of Pt–Ni/rGO nanocatalysts synthesized in the typical experiments. **e** HRTEM, high-angle annular dark-field (HAADF)-STEM-EDX of **f** line-scanning profiles and **g**, **h** mappings of an individual Pt–Ni alloy nanoparticle (PNANP) on rGO.

Inset of **b** and **f** are the diameter distribution of Pt–Ni alloy nanoparticles (PNANPs) on rGO, and HAADF-STEM image of an individual PNANP, respectively. Meanwhile, PNANP and rGO are indicated by the white circle and red arrow in **b**, respectively

which appear at 285.8, 286.5, 287.8, and 289.1 eV are assigned to the contributions from C–N, C=O (carbonyl group), C–O (epoxy, alcohol, and ester), and O–C=O (carboxyl group), respectively. These results mean that GO is effectively reduced to rGO (Shi et al. 2018). The high-resolution Pt 4f spectrum in Fig. 4d is divided into the four diffraction peaks consisting of two strong ones for Pt at 70.6 eV (Pt $4f_{7/2}$) and 73.9 eV (Pt $4f_{5/2}$), with other weak ones that are ascribed to platinic oxide and

platinic hydroxide (Fernández et al. 2016), respectively. Specifically, metallic platinum is dominant, implying that Pt^{4+} ions are effectively reduced to Pt atoms in our hydrothermal approach. Therefore, our work can supply more active sites for desorption of hydrogen atom than Pt^{2+} and enhance catalytic performance for the typical samples towards HER as well. The Ni 2p spectrum of the typical samples (curve B, Fig. 5) demonstrates the strong peak of $Ni(OH)_2$ at 856.3 eV, as well as that of
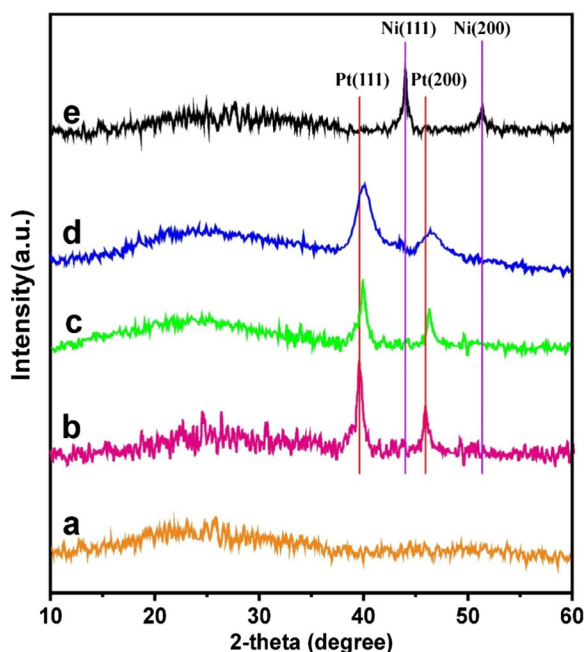
Fig. 2 XRD patterns of (a) rGO and metal/rGO nanocatalysts synthesized at various F values of (b) 1:0, (c) 3:1, (d) 3:2, and (e) 0:1

Ni(0) at 853.2 eV (Choi et al. 2014), suggesting the formation of nickel hydroxide on the typical samples. No nickel oxide (NiO) is found in curve B of Fig. 5. Generally, nickel hydroxide on the as-synthesized nanocatalyst cannot decompose to NiO and H_2O in our experimental condition unless the reaction temperature is no less than 230 °C (Biesinger et al. 2011). Associated with XRD pattern of the typical samples (Fig. 1d), the peak of $Ni(OH)_2$ is not detected in this figure, indicative of noncrystalline hydroxide (Choi et al. 2013). In order to confirm our opinion, we further investigate XPS of Ni species on the surface of the typical samples after the HAc treatment (Pt–Ni(1:1)/rGO-HAc). The intensity ratio of $Ni(OH)_2$ to Ni(0) for Pt–Ni(1:1)/rGO-HAc (curve C, Fig. 5) is observed to decrease significantly compared to that of the typical samples, indicating the partially selective etching of $Ni(OH)_2$. However, the spectrum of the typical samples after 0.1 M KOH solution treatment (Pt–Ni(1:1)/rGO-KOH) (curve A, Fig. 5) does not display the significant change in comparison with the typical samples, implying that $Ni(OH)_2$ is naturally formed on the surface of our samples. Consequently, we conclude that Ni species on the surface of the typical nanocatalysts should be $Ni(OH)_2$.

Figure 6a presents the Raman spectra of GO, rGO, and the typical samples. All samples demonstrate two prominent peaks at about 1341 and 1595 cm^{-1}, which match exactly with the well-documented G band and D band, respectively (Hu et al. 2011). According to the reported literature (Graf et al. 2007), the level of graphitization of carbonaceous materials or defect density is usually detected by the signal ratio of D band to G band (I_D/I_G). Meanwhile, I_D/I_G ratios for GO, rGO, and the typical samples are about 1.00, 1.21, and 1.28, respectively. I_D/I_G of rGO and the typical samples are higher than that for GO, which implies that the new domains of conjugated carbon atoms are generated owing to the removal of the oxygenous groups (Li et al. 2015). On the other hand, the I_D/I_G ratio for the typical samples slightly increases, confirming that the structure of graphene is well preserved even after deposition of Pt–Ni alloy NPs (Li et al. 2014). This is important to achieve good electrical conductivity for design of such our hybrid system as electrocatalysts. The reduction of the oxygen-containing groups in GO is also confirmed by Fourier-transforming infrared (FT-IR) spectroscopy. Broad and intense peak at 3409 cm^{-1} or so is responsible for the O–H stretching vibration of C–OH and water in Fig. 6b (curve A for GO) (Li et al. 2014). The stretching vibration of C=O in carbonyl or carboxylic groups is responsible for the weak peak at about 1735 cm^{-1}. The peak at ~ 1620 cm^{-1} is related to the vibrations of the absorbed water molecules and the skeletal vibration of unoxidized graphitic domains (Yang et al. 2014). The peaks at approximately 1384, 1224, and 1053 cm^{-1} are associated with the deformation of the O–H groups and the stretching vibration of C–O in the epoxy and alkoxy groups (Kim et al. 2011), respectively. After the reduction reaction, FT-IR patterns (curve B and curve C, Fig. 6b) for rGO and the typical samples are quite different from that of GO, confirming that the oxygen-containing functional groups are significantly removed from rGO and the typical samples. Furthermore, the formation of Pt–Ni alloy NPs supported on rGO is also characterized by UV-visible spectroscopy. In the adsorption spectrum of GO (Fig. 6c, curve A), the adsorption peak at about 230 nm can be attributed to the π–π* transition of aromatic C=C bond (Lu et al. 2013). Nevertheless, after the hydrothermal approach with the metal precursors, a peak centered at about 270 nm appears for the typical samples, accompanied with the red shift of the adsorption peak at 230 nm, which is almost same as the wavelength of absorption peak of rGO (Fig. 6c,
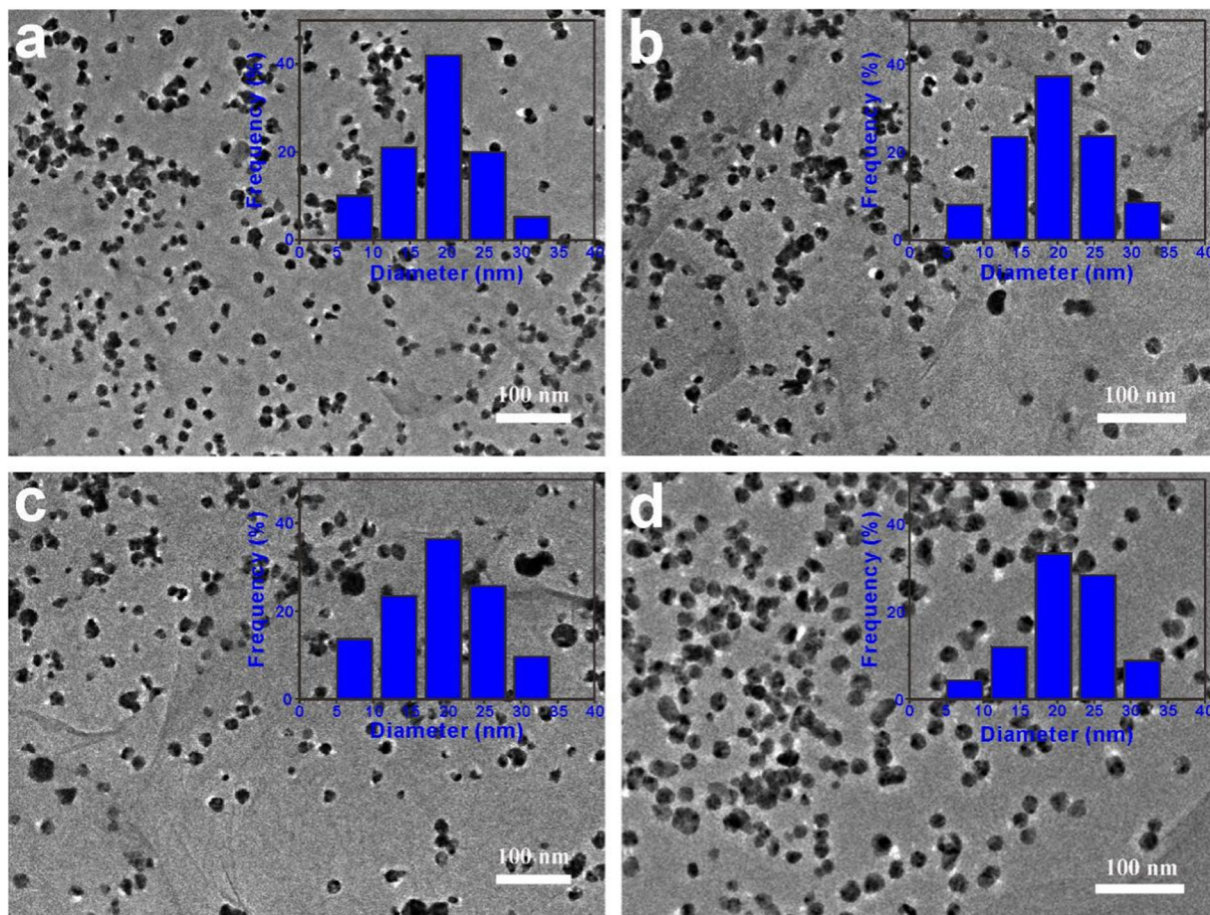
Fig. 3 TEM images of metal/rGO nanocatalysts synthesized at various F values of **a** 1:0, **b** 3:1, **c** 3:2, and **d** 0:1

curve B). These results further indicate the formation of rGO in the typical samples (Fig. 6c, curve C) (Lu et al. 2013). Thermogravimetric analysis (TGA) is conducted to quantitatively analyze the weight percentage of metal loading of Pt–Ni(1:1)/rGO. According to curve A of Fig. 6d for GO, the major weight losses are observed at approximately 100, 200, and 450 °C, which originate from the escape of water molecules absorbed between GO, thermal decomposition of oxygen-containing groups, and combustion of carbon skeleton, respectively (Shi et al. 2018). In contrast with curve A of Fig. 6d, the weight loss of rGO (Fig. 6d, curve B) or the typical samples (Fig. 6d, curve C) at about 200 °C is much lower than that of GO under the same conditions, suggesting the significant decrease in the quantity of oxygen-containing functional groups on rGO (Darabdhara et al. 2015; Li et al. 2013b). In addition, the percentage of PNANPs by weight is about 40% for the typical samples.

Magnetic properties and magnetic recollection of the typical Pt–Ni/rGO nanocatalysts

As a magnetically recoverable catalyst, Ni may exhibit less activity towards HER by the electrochemical method. It is usually coupled with Pt to improve its catalytic activity (Sahoo et al. 2014). However, Ni alloyed with some noble metals would lose its intrinsic ferromagnetism due to the incorporation of other heteroatoms into Ni lattices. This would largely damage the magnetic recollection or recoverability of Ni-based alloy. As we know, the nickel-rich Pt–Ni alloy is ferromagnetic (Parra and Cable 1980). Therefore, the formation of Pt–Ni alloy NPs on rGO here can also be reflected from their magnetic properties. As is shown in Fig. 7a, Pt–Ni(1:1)/rGO nanocatalysts present typical ferromagnetic hysteresis curve which reaches saturation about 5.0 kOe magnetic fields at room temperature. From this figure, Ms of the typical samples is 6.1 emu g^{-1}. In
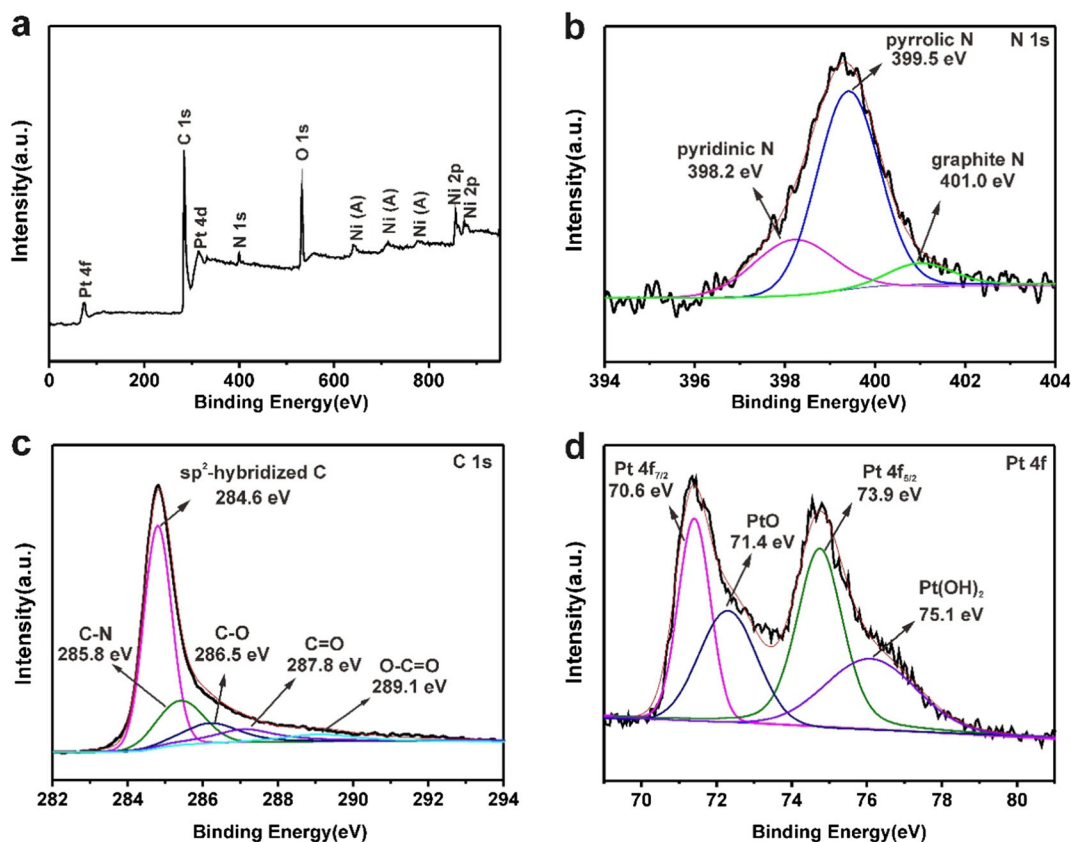
Fig. 4 XPS spectra of the typical Pt–Ni/rGO nanocatalysts: **a** full spectrum, **b** N 1s, **c** C 1s, and **d** Pt 4f high-resolution spectra

addition, the enlarged *M-H* loops (inset of Fig. 7a) indicate that our samples exhibit high *H*c (128.5 Oe) and low *M*r (1.15 emu g^{-1}) in comparison with bulk Ni (~ 0.7 Oe and 2.7 emu g^{-1}). Although *M*s of the typical samples is much lower than that of bulk Ni (55 emu g^{-1}) (Liu et al. 2010), the *M*s could be still large enough for magnetic separation from the reaction system by a magnet. Figure 7b demonstrates the easy manipulation (within ~ 6 s) of the typical nanocatalysts by placing an external magnet outside the bottle, indicating the excellent magnetic recollection of our nanocatalysts after their fabrication.

Electrocatalytic HER performances of Pt–Ni/rGO nanocatalysts

The electrocatalytic performances of various nanocatalysts towards HER are evaluated in Fig. 8 in alkaline media using a typical three-electrode system. Herein, the rGO-supported various Pt–Ni alloys or metal NPs result in the greatly differences in their HER

performances. Figure 8a, b shows polarization curves and Tafel plots of the rGO-supported various metal NPs in comparison with those of commercial Pt/C catalysts. As is shown in Fig. 8a, the overpotential of the typical samples is as low as − 78 mV or so at a current density of 10 mA cm^{-2}. In contrast, those of the commercial Pt/C and Pt/rGO catalysts reach up to − 124 and − 149 mV at the same condition, respectively. It is worth noting that Ni/rGO catalysts show the relatively low HER activity in our experiments, such as its overpotential reaching − 231 mV or so under the same condition, thereby suggesting that the active species of our nanocatalysts come from Pt atoms rather than nickel ones or nickel hydroxide. More importantly, HER activities of Pt–Ni/rGO nanocatalysts increase gradually with the decrease of *F*. For example, at a current density of 10 mA cm^{-2}, Pt–Ni(3:1)/rGO and Pt–Ni(3:2)/rGO nanocatalysts exhibit the overpotential of − 120 and − 112 mV, respectively. This implies the occurrence of a synergistic interaction between Pt and Ni for this kind of bimetallic nanocatalysts in our work. Tafel slope is the intrinsic
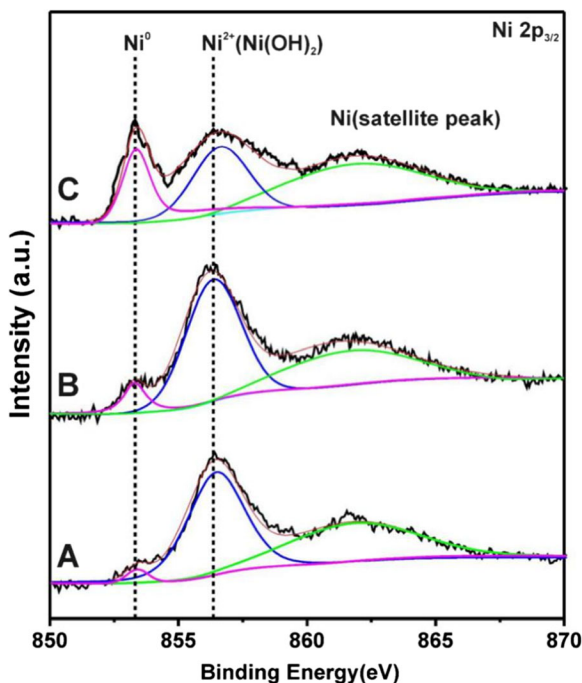
Fig. 5 Comparison of Ni 2p high-resolution XPS spectra for the typical samples (curve B) and the typical samples after KOH (curve A) and HAc treatments (curve C). Pt–Ni(1:1)/rGO-KOH and Pt–Ni(1:1)/rGO-HAc are obtained by treating the typical samples with 0.1 M KOH solution at room temperature for 1 h and with HAc at 60 °C for 30 min, respectively

parameter of an electrocatalyst, which depends on the rate-controlling step during production of hydrogen by electrochemical technology (Yang et al. 2017). In alkaline condition, the Volmer reaction, $H_2O + e + M = M–H_{ads} + OH^-$, is considered as a rate-controlling step, owing to the slow dynamics of decomposition of water. From Fig. 8b, the commercial Pt/C, Pt/rGO, and Ni/rGO catalysts give rise to Tafel slopes of ~ 78, ~ 88, and ~ 125 mV/dec, respectively, while the typical samples also exhibit the smallest Tafel slope among all samples, about 53 mV/dec. Herein, nickel hydroxide layer on our nanocatalysts can promote the decomposition of water in basic condition (Yin et al. 2015; Yang et al. 2017; Subbaraman et al. 2011, 2012), which is one of the important factors to improve electrocatalytic performance of Pt–Ni hybrid materials. The determination of the electrochemical surface area (ECSA) of electrocatalyst is described in Electronic Supplementary Material according to the related literature (Kavian et al. 2016). For the typical samples, Figs. S2a and S3a exhibit distinct hydrogen adsorption/desorption on Pt surface, and the oxidation and reduction of Ni (red area),

respectively. The specific ECSA value of the typical samples determined by hydrogen desorption area (yellow area of Fig. S2a or 8c) in 1.0 M KOH solution is about 35.2 ± 2.4 m^2 g^{-1}. The specific ECSA value of the commercial Pt/C catalysts increases to about 52.1 ± 3.6 m^2 g^{-1} (Fig. 8c), which approaches to that of Pt/rGO catalysts (54.5 ± 3.8 m^2 g^{-1}, Fig. 8c). These results indicate the relatively high Pt loading amount of the commercial Pt/C or Pt/rGO catalysts compared to the typical samples, thereby indicating that more Pt atoms are exposed on their corresponding working electrodes. The specific HER activities of these catalysts are calculated by normalizing the reduction currents at -0.1 V vs. RHE to their corresponding ECSAs. The specific HER activity of the typical samples demonstrates the superior catalytic performance among all samples, reaches up to 1.09 ± 0.08 mA cm$^{-2}_{Pt}$, a value about three and five times higher than those of the commercial Pt/C (0.28 ± 0.02 mA cm$^{-2}_{Pt}$) and Pt/rGO catalysts (0.21 ± 0.02 mA cm$^{-2}_{Pt}$, Fig. 8d or Table S2), respectively. Subsequently, HER activity in low concentration KOH solution is displayed in Fig. 9. According to Fig. 9a, the overpotentials of the typical samples and the commercial Pt/C are -119 and -147 mV, respectively. Therefore, HER activities of the typical samples are also higher than those of commercial Pt/C ones.

In order to determine the long-term durability of electrocatalyst, polarization curves of Pt–Ni(1:1)/rGO nanocatalysts are recorded before and after scanning for 1000 scans (Su et al. 2016). As expected, Eonset value is almost unchanged and the increase in overpotential is as low as about 2 mV at a current density of 20 mA cm^{-2} before and after this test (Fig. 10a). Furthermore, the current loss for 8 h is also negligible because the current density ranges from -10.0 to -9.7 mA cm^{-2} (Fig. 10b), indicating the excellent stability of the typical samples.

Possible catalytic mechanism

In our work, the diameter of metal nanoparticles should have no significant effect on HER activity of electrocatalysts. This is because the metal nanoparticles on rGO synthesized at various F almost have the same diameter, as shown in Figs. 1b and 3. Additionally, the diameter of Pt nanoparticles for the commercial Pt/C catalysts is less than 3.5 nm which is provided by the manufacturers. Herein, we speculated that the highest HER activity of Pt–Ni(1:1)/rGO nanocatalysts among
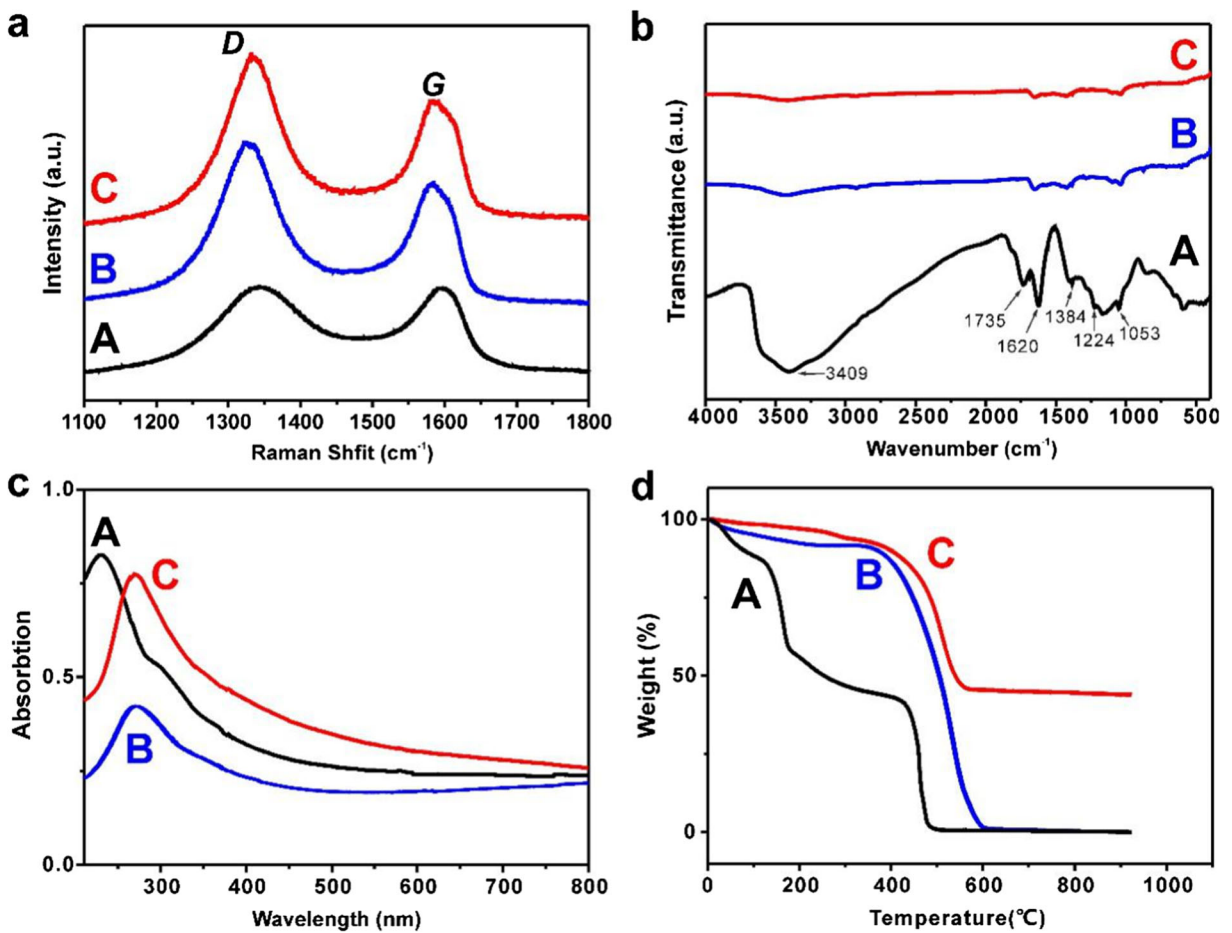
Fig. 6 **a** Raman spectra, **b** FT-IR spectra, **c** UV-visible absorption, and **d** TGA curves of (A) GO, (B) rGO, and (C) the typical samples

all samples (Fig. 8) is not only attributed to Ni(OH)$_2$ of PNANPs facilitating the decomposition of water in basic condition, but also ascribed to the synergistic interaction between Pt and Ni for our hybrid systems.
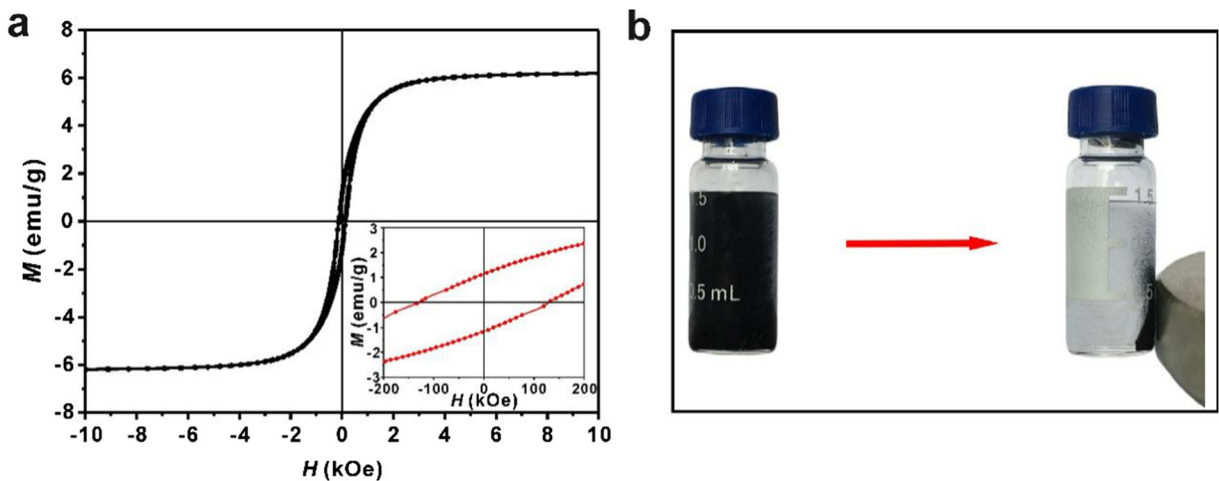

Fig. 7 **a** Hysteresis loops and **b** illustration for the magnetic separation of the typical samples. Inset of **a** shows the magnified H region from − 250 to 250 Oe
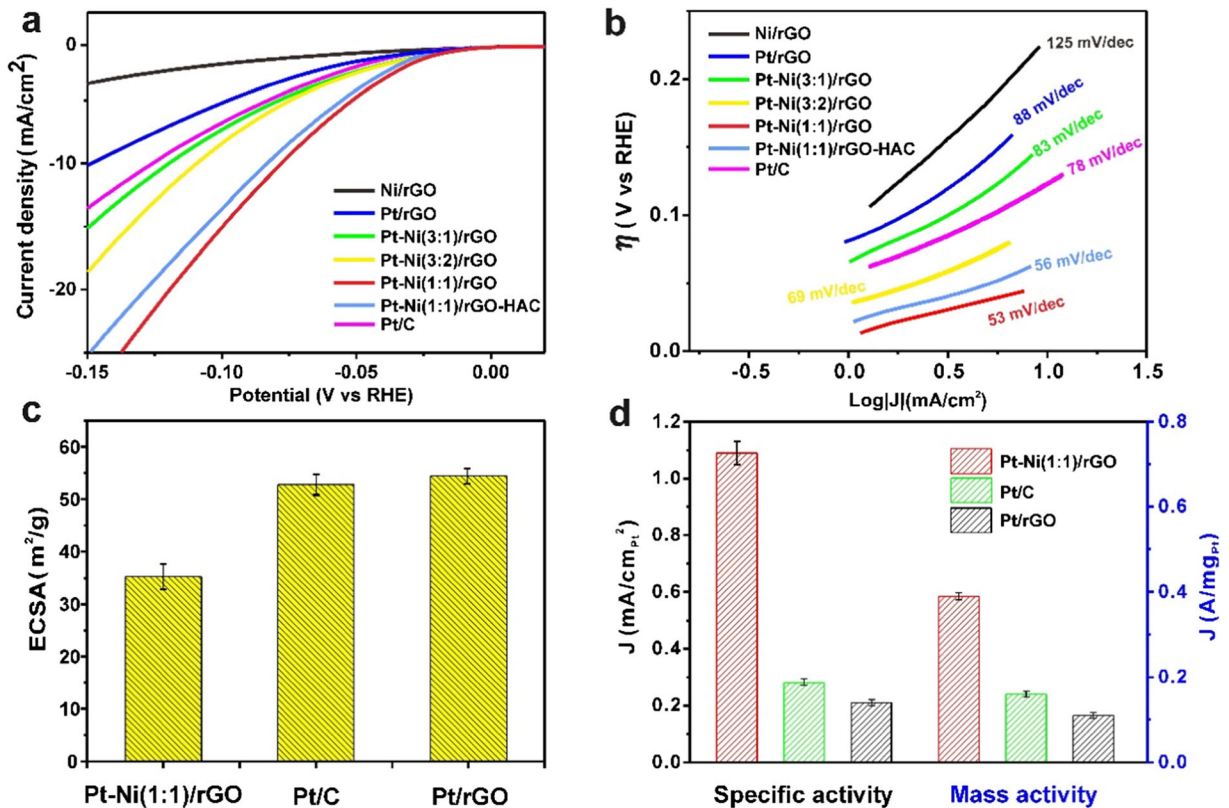
Fig. 8 a Polarization curves and **b** Tafel plots of metal/rGO nanocatalysts synthesized at various Pt^{4+}/Ni^{2+} molar ratios, Pt–Ni(1:1)/rGO-HAc, and commercial Pt/C catalysts for HER with a scan rate of 5 mV s^{-1}; comparison of **c** ECSAs and **d** specific activities and mass activities of the typical samples, the commercial Pt/C, and Pt/rGO catalysts. The electrolyte is N_2-saturated 1.0 M KOH. Meanwhile, the actual Pt loading amount of the commercial Pt/C, Pt/rGO, Pt–Ni(3:1)/rGO, Pt–Ni(3:2)/rGO, and Pt–Ni(1:1)/rGO in their corresponding working electrodes are 3.83, 3.64, 3.32, 3.01, and 2.92 μg, respectively

Possible catalytic mechanism of the typical samples for HER in alkaline media is illustrated in Fig. 11. In order to confirm our speculation, we further investigate HER activity of Pt–Ni(1:1)/rGO-HAc in Fig. 8a, b. For
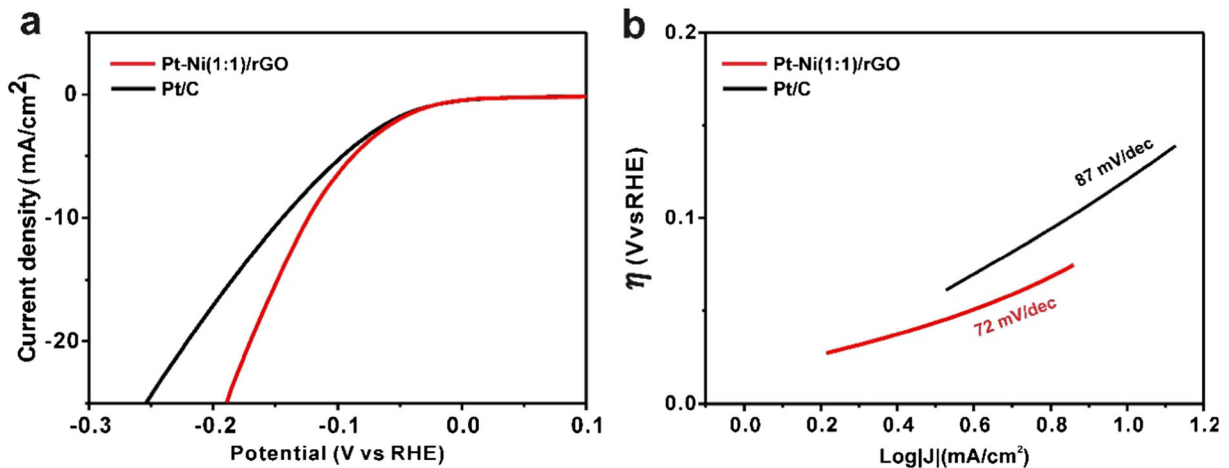

Fig. 9 a Polarization curves and **b** Tafel plots of the typical samples and commercial Pt/C (20 wt%) for HER with a scan rate of 5 mV s^{-1} in N_2-saturated 0.1 M KOH, other conditions as Fig. 8
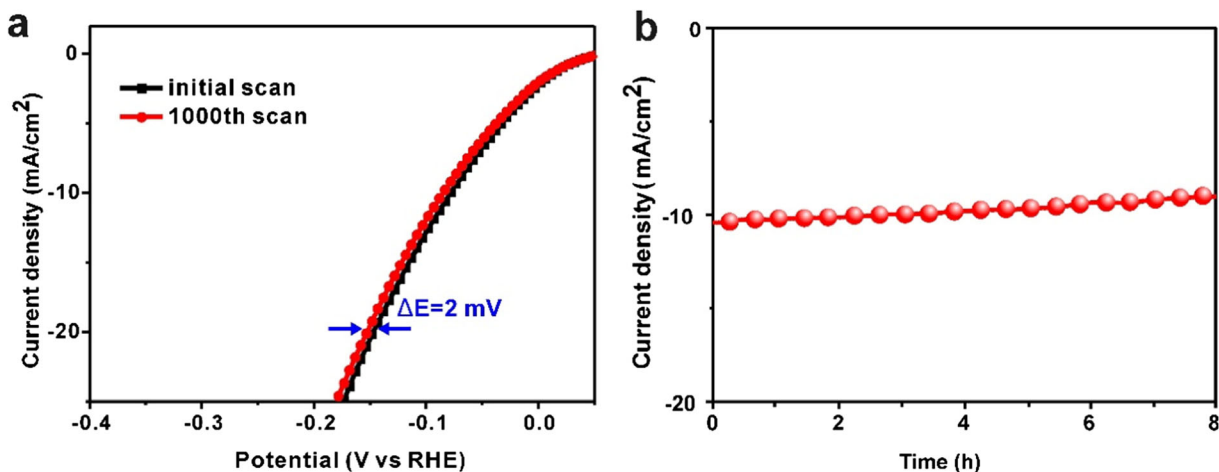
Fig. 10 **a** Polarization curves of the typical samples before and after 1000 cycles for a durability test and **b** time-dependent current density curve for the typical samples under a static overpotential of − 78 mV for 8 h, other conditions as Fig. 8

example, the overpotential of Pt–Ni(1:1)/rGO-HAc increases to − 82 mV at a current density of 10 mA cm^{-2}, and their Tafel slope, 56 mV/dec, is also higher than that of the typical samples, due to the partially selective etching nickel hydroxide on Pt–Ni(1:1)/rGO-HAc. For the typical Pt–Ni/rGO samples, sufficient nickel hydroxide could efficiently activate the HO–H bond, which facilitates the decomposition of water in basic condition for HER (Yin et al. 2015; Subbaraman et al. 2011; Chen et al. 2014). On the other hand, nickel content-dependent electrocatalytic activities of as-synthesized nanocatalysts for HER in Fig. 6 can be explained as modifying the electronic structure of

platinum by nickel because of the electron transfer from the active metal to the inert one. Therefore, it results in the relatively low density of states at the Fermi level to Pt (Hu et al. 2012; Li et al. 2013a), and could decrease the bond energy between Pt atoms and H ones, and improve desorption of hydrogen atoms on our nanocatalysts as well. Consequently, the typical samples present higher electrocatalytic activity than the commercial Pt/C and Pt/rGO ones.

In addition, nickel hydroxide layer on our nanocatalysts could effectively protect them against corrosion in strong basic environment. Therefore, the typical samples present excellent HER catalytic stability.
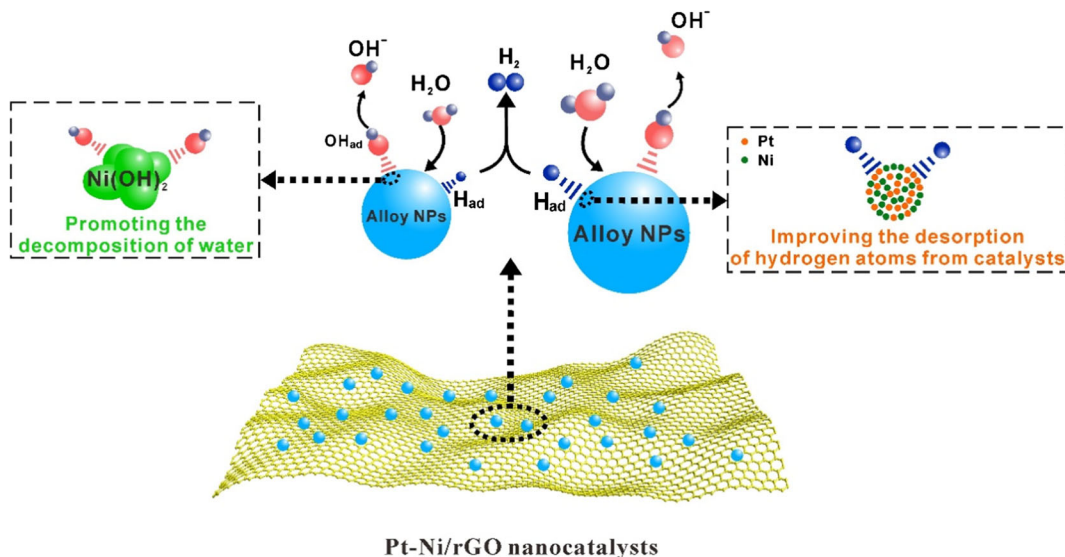

Fig. 11 Schematic illustration of possible catalytic mechanism of Pt–Ni/rGO nanocatalysts for HER in alkaline media

Conclusions

In this work, we have demonstrated a facile design strategy to prepare the rGO-supported Pt–Ni alloy NPs with $Ni(OH)_2$ naturally formed on their surfaces as excellent electrocatalysts for HER in alkaline environment. In this work, the structure and composition of electrocatalysts can be effectively controlled by simply changing F. Specially, the diffraction peaks of the as-synthesized nanocatalysts gradually convert to Ni ones while F decreases, suggesting that a series of Pt–Ni alloy NPs on rGO are achieved. In addition, XPS analysis reveals that nickel species on the typical Pt–Ni/rGO nanocatalysts tend to be oxidized to $Ni(OH)_2$ form during the hydrothermal fabrication. Based on the design for such hybrid materials, the typical nanocatalysts demonstrate the superior electrocatalytic activities towards HER among all samples. The performance improvement reasonably illustrated the following two points: (1) the introduction of nickel hydroxide layer on our nanocatalysts can promote the decomposition of water in basic condition and (2) the improvement in the electronical feature of platinum atoms by nickel ones leads to the relatively low density of states at the Fermi level to Pt, which could decrease the bond energy between Pt atoms and H ones and improve the desorption of hydrogen atoms on our nanocatalysts as well. Furthermore, $Ni(OH)_2$ layer for our nanocatalysts can effectively protect them against corrosion, and thus, the typical samples present excellent HER catalytic stability. The advance of our work greatly decreases the Pt utilization and enhances the electrocatalytic activity, and owns excellent stability and magnetic recollection as well. This work will promise the important application in the aspect of high-performance and cost-effective Pt-based electrocatalysts in alkaline electrolyte.

Authors' contributions Zuokai Du performed most experiments and collected and analyzed data in the original manuscript. Yilong Wang and Jinping Liu participated in the design of this work. Junsheng Li is listed as one of coauthors, as he did some experiments and the related characterization of the as-synthesized nanocatalysts for this revised manuscript. Manuscript was written by Yilong Wang, and critically reviewed by Jinping Liu. All authors read and approved the final manuscript.

Compliance with ethical standards

Conflict of interest The authors declare that they have no conflict of interest.

Publisher's Note Springer Nature remains neutral with regard to jurisdictional claims in published maps and institutional affiliations.

References

Bao X, Wang J, Lian X, Jin H, Wang S, Wang Y (2017) Ni/ nitrogen-doped graphene nanotubes acted as a valuable tailor for remarkably enhanced hydrogen evolution performance of platinum-based catalysts. J Mater Chem A 5:16249–16254

Bian J, Lan F, Wang Y, Ren K, Zhao S, Li W, Chen Z, Li J, Guan J (2018) Facile morphology-controlled synthesis of nickel-coated graphite core-shell particles for excellent conducting performance of polymer-matrix composites and enhanced catalytic reduction of 4-nitrophenol. Nanotechnology 29: 145602

Biesinger MC, Payne BP, Grosvenor AP, Lau LWM, Gerson AR, Smart RSC (2011) Resolving surface chemical states in XPS analysis of first row transition metals, oxides and hydroxides: Cr, Mn, Fe, Co and Ni. Appl Surf Sci 257:2717–2730

Chen S, Sheng WC, Yabuuchi N, Ferreira PJ, ALFaYS H (2009) Origin of oxygen reduction reaction activity on "Pt$_3$Co" nanoparticles: atomically resolved chemical compositions and structures. J Phys Chem C 113:1109–1125

Chen C, Kang Y, Huo Z, Zhu Z, Huang W, Xin HL, Snyder JD, Li D, Herron JA, Mavrikakis M, Chi M, More KL, Li Y, Markovic NM, Somorjai GA, Yang P, Stamenkovic VR (2014) Highly crystalline multimetallic nanoframes with three-dimensional electrocatalytic surfaces. Science 343: 1339–1343

Chen Y, Chen Y, Yu G, Chen W, Liu Y, Li GD, Zhu P, Tao Q, Li Q, Liu J, Shen X, Li H, Huang X, Wang D, Asefa T, Zou X (2017) Highly active, nonprecious electrocatalyst comprising borophene subunits for the hydrogen evolution reaction. J Am Chem Soc 139:12370–12373

Choi SI, Xie S, Shao M, Odell JH, Lu N, Peng HC, Protsailo L, Guerrero S, Park J, Xia X, Wang J, Kim MJ, Xia Y (2013) Synthesis and characterization of 9 nm Pt-Ni octahedra with a record high activity of 3.3 A/mg$_{Pt}$ for the oxygen reduction reaction. Nano Lett 13:3420–3425

Choi S-I, Shao M, Lu N, Ruditskiy A, Peng H, Park J, Guerrero S, Wang J, Kim M, Xia Y (2014) Synthesis and characterization of Pd@Pt-Ni core-shell octahedra with high activity toward oxygen reduction. ACS Nano 8:10363–10371

Darabdhara G, Amin MA, Mersal GAM, Ahmed EM, Das MR, Zakaria MB, Malgras V, Alsheri SM, Yamauchi Y, Szunerits S, Boukherroub R (2015) Reduced graphene oxide nanosheets decorated with Au, Pd and Au–Pd bimetallic nanoparticles as highly efficient catalysts for electrochemical hydrogen generation. J Mater Chem A 3:20254–20266

Fan X, Zhang G, Zhang F (2015) Multiple roles of graphene in heterogeneous catalysis. Chem Soc Rev 44:3023–3035

Fang Z, Hao Z, Dong Q, Cui Y (2018) Bimetallic NiFe$_2$O$_4$ synthesized via confined carburization in NiFe-MOFs for efficient oxygen evolution reaction. J Nanopart Res 20:106

Fernández A, Arzac GM, Vogt UF, Hosoglu F, Borgschulte A, Jiménez de Haro MC, Montes O, Züttel A (2016) Investigation of a Pt containing washcoat on SiC foam for hydrogen combustion applications. Appl Catal B Environ 180:336–343

Graf D, Molitor F, Ensslin K, Stampfer C, Jungen A, Hierold C, Wirtz L (2007) Spatially resolved raman spectroscopy of single- and few-layer graphene. Nano Lett 7:238–242

Hao Z, Yang S, Niu J, Fang Z, Liu L, Dong Q, Song S, Zhao Y (2018) A bimetallic oxide Fe$_{1.89}$Mo$_{4.11}$O$_7$ electrocatalyst with highly efficient hydrogen evolution reaction activity in alkaline and acidic media. Chem Sci 9:5640–5645

He T, Kreidler E, Xiong L, Ding E (2007) Combinatorial screening and nano-synthesis of platinum binary alloys for oxygen electroreduction. J Power Sources 165:87–91

Hu C, Cao Y, Yang L, Bai Z, Guo Y, Wang K, Xu P, Zhou J (2011) Preparation of highly dispersed Pt-SnO$_X$ nanoparticles supported on multi-walled carbon nanotubes for methanol oxidation. Appl Surf Sci 257:7968–7974

Hu Y, Wu P, Yin Y, Zhang H, Cai C (2012) Effects of structure, composition, and carbon support properties on the electrocatalytic activity of Pt-Ni-graphene nanocatalysts for the methanol oxidation. Appl Catal B Environ 111-112:208–217

Kavian R, Choi S-I, Park J, Liu T, Peng HC, Lu N, Wang J, Kim MJ, Xia Y, Lee SW (2016) Pt–Ni octahedral nanocrystals as a class of highly active electrocatalysts toward the hydrogen evolution reaction in an alkaline electrolyte. J Mater Chem A 4:12392–12397

Kim H, Namgung R, Singha K, Oh IK, Kim WJ (2011) Graphene oxide-polyethylenimine nanoconstruct as a gene delivery vector and bioimaging tool. Bioconjug Chem 22:2558–2567

Konopka DA, Li M, Artyushkova K, Marinkovic N, Sasaki K, Adzic R, Ward TL, Atanassov P (2011) Platinum supported on NbRu$_y$O$_z$ as electrocatalyst for ethanol oxidation in acid and alkaline fuel cells. J Phys Chem C 115:3043–3056

Kou R, Shao Y, Mei D, Nie Z, Wang D, Wang C, Viswanathan VV, Park S, Aksay IA, Lin Y, Wang Y, Liu J (2011) Stabilization of electrocatalytic metal nanoparticles at metal-metal oxide-graphene triple junction points. J Am Chem Soc 133:2541–2547

Kwon S, Hyeon T (2011) Formation mechanisms of uniform nanocrystals via hot-injection and heat-up methods. Small 7:2685–2702

Li L, Wu Y, Lu J, Nan C, Li Y (2013a) Synthesis of Pt-Ni/graphene via in situ reduction and its enhanced catalyst activity for methanol oxidation. Chem Commun 49:7486–7488

Li F, Guo Y, Li R, Wu F, Liu Y, Sun X, Li C, Wang W, Gao J (2013b) A facile method to synthesize supported Pd–Au nanoparticles using graphene oxide as the reductant and their extremely high electrocatalytic activity for the electrooxidation of methanol and ethanol. J Mater Chem A 1:6579–6587

Li SS, Lv JJ, Hu YY, Zheng JN, Chen JR, Wang AJ, Feng JJ (2014) Facile synthesis of porous Pt–Pd nanospheres supported on reduced graphene oxide nanosheets for enhanced methanol electrooxidation. J Power Sources 247:213–218

Li J, Zhou P, Li F, Ren R, Liu Y, Niu J, Ma J, Zhang X, Tian M, Jin J, Ma J (2015) Ni@Pd/PEI–rGO stack structures with controllable Pd shell thickness as advanced electrodes for efficient hydrogen evolution. J Mater Chem A 3:11261–11268

Liu L, Guan J, Shi W, Sun Z, Zhao J (2010) Facile synthesis and growth mechanism of flowerlike Ni-Fe alloy nanostructures. J Phys Chem C 114:13565–13570

Liu Y, Yu G, Li GD, Sun Y, Asefa T, Chen W, Zou X (2015) Coupling Mo$_2$C with nitrogen-rich nanocarbon leads to efficient hydrogen-evolution electrocatalytic sites. Angew Chem Int Ed 54:10752–10757

Liu L, Chen R, Liu W, Wu J, Gao D (2016) Catalytic reduction of 4-nitrophenol over Ni-Pd nanodimers supported on nitrogen-doped reduced graphene oxide. J Hazard Mater 320:96–104

Liu Y, Li Q, Si R, Li G, Li W, Liu D, Wang D, Sun L, Zhang Y, Zou X (2017) Coupling sub-nanometric copper clusters with quasi-amorphous cobalt sulfide yields efficient and robust electrocatalysts for water splitting reaction. Adv Mater 29:1606200

Liu Y, Liang X, Gu L, Zhang Y, Li G, Zou X, Chen J (2018) Corrosion engineering towards efficient oxygen evolution electrodes with stable catalytic activity for over 6000 hours. Nat Commun 9:2609

Loukrakpam R, Luo J, He T, Chen Y, Xu Z, Njoki PN, Wanjala BN, Fang B, Mott D, Yin J, Klar J, Powell B, Zhong C (2011) Nanoengineered PtCo and PtNi catalysts for oxygen reduction reaction: an assessment of the structural and electrocatalytic properties. J Phys Chem C 115:1682–1694

Lu Y, Jiang Y, Wu H, Chen W (2013) Nano-PtPd cubes on graphene exhibit enhanced activity and durability in methanol electrooxidation after CO stripping–cleaning. J Phys Chem C 117:2926–2938

Lv R, Li Q, Botello-Méndez AR, Hayashi T, Wang B, Berkdemir A, Hao Q, Elias AL, Cruz-Silva R, Gutierrez HR, Kim YA, Muramatsu H, Zhu J, Endo M, Terrones H, Charlier JC, Pan M, Terrones M (2012) Nitrogen-doped graphene: beyond single substitution and enhanced molecular sensing. Sci Rep 2:586

Mezzavilla S, Baldizzone C, Swertz AC, Hodnik N, Pizzutilo E, Polymeros G, Keeley GP, Knossalla J, Heggen M, Mayrhofer KJJ, Schüth F (2016) Structure–activity–stability relationships for space-confined Pt$_x$Ni$_y$ nanoparticles in the oxygen reduction reaction. ACS Catal 6:8058–8068

Parra RE, Cable JW (1980) Neutron study of magnetic-moment distribution in Ni-Pt alloys. Phys Rev B 21:5494–5504

Pylypenko S, Borisevich A, More KL, Corpuz AR, Holme T, Dameron AA, Olson TS, Dinh HN, Gennett T, O'Hayre R (2013) Nitrogen: unraveling the secret to stable carbon-supported Pt-alloy electrocatalysts. Energy Environ Sci 6:2957

Sahoo PK, Panigrahy B, Bahadur D (2014) Facile synthesis of reduced graphene oxide/Pt–Ni nanocatalysts: their magnetic and catalytic properties. RSC Adv 4:48563–48571

Shi YC, Chen SS, Feng JJ, Xiao LX, ping WW, Jun WA (2018) Dicationic ionic liquid mediated fabrication of Au@Pt nanoparticles supported on reduced graphene oxide with highly catalytic activity for oxygen reduction and hydrogen evolution. Appl Surf Sci 441:438–447

Su S, Zhang C, Yuwen L, Liu X, Wang L, Fan C, Wang L (2016) Uniform Au@Pt core-shell nanodendrites supported on molybdenum disulfide nanosheets for the methanol oxidation reaction. Nanoscale 8:602–608

Subbaraman R, Tripkovic D, Strmcnik D, Chang KC, Uchimura M, Paulikas AP, Stamenkovic V, Markovic NM (2011)

Enhancing hydrogen evolution activity in water splitting by tailoring Li^+-$Ni(OH)_2$-Pt interfaces. Science 334:1256–1260

Subbaraman R, Tripkovic D, Chang KC, Strmcnik D, Paulikas AP, Hirunsit P, Chan M, Greeley J, Stamenkovic V, Markovic NM (2012) Trends in activity for the water electrolyser reactions on 3d M(Ni,Co,Fe,Mn) hydr(oxy)oxide catalysts. Nat Mater 11:550–557

Tang L, Wang Y, Li Y, Feng H, Lu J, Li J (2009) Preparation, structure, and electrochemical properties of reduced graphene sheet films. Adv Funct Mater 19:2782–2789

Wang ZB, Zhao CR, Shi PF, Yang YS, Yu ZB, Wang WK, Yin GP (2010) Effect of a carbon support containing large mesopores on the performance of a Pt-Ru-Ni/C catalyst for direct methanol fuel cells. J Phys Chem C 114:672–677

Wang X, Sun G, Routh P, Kim DH, Huang W, Chen P (2014) Heteroatom-doped graphene materials: syntheses, properties and applications. Chem Soc Rev 43:7067–7098

Wang Y, Wen J, Zhao S, Chen Z, Ren K, Sun J, Guan J (2015) Surface thiolation of Al microspheres to deposit thin and compact Ag shells for high conductivity. Langmuir 31: 13441–13451

Wang Y, Luo S, Ren K, Zhao S, Chen Z, Li W, Guan J (2016) Facile preparation of graphite particles fully coated with thin Ag shell layers for high performance conducting and electromagnetic shielding composite materials. J Mater Chem C 4: 2566–2578

Wang Y, Ren K, Sun J, Li W, Zhao S, Chen Z, Guan J (2017) Ultralow content silver densely-coated glass microsphere for high performance conducting polymer-matrix composites. Compos Sci Technol 140:89–98

Wu X, Fan Z, Ling X, Wu S, Chen X, Hu X, Zhuang N, Chen J (2018) Enhanced lithium-ion storage and hydrogen evolution reaction catalysis of MoS_2/graphene nanoribbons hybrids with loose interlaced three-dimension structure. J Nanopart Res 20:156

Xu Y, Li Y, Yin S, Yu H, Xue H, Li X, Wang H, Wang L (2018) Ultrathin nitrogen-doped graphitized carbon shell encapsulating CoRu bimetallic nanoparticles for enhanced electrocatalytic hydrogen evolution. Nanotechnology 29:225403

Yang YW, Feng G, Lu ZH, Hu N, Zhang F, Chen XS (2014) In situ synthesis of reduced graphene oxide supported Co nanoparticles as efficient catalysts for hydrogen generation from NH_3BH_3. Acta Phys-Chim Sin 30:1180–1186

Yang H, Wang C, Hu F, Zhang Y, Lu H, Wang Q (2017) Atomic-scale Pt clusters decorated on porous α-$Ni(OH)_2$ nanowires as highly efficient electrocatalyst for hydrogen evolution reaction. Sci China Mater 60:1121–1128

Yin H, Zhao S, Zhao K, Muqsit A, Tang H, Chang L, Zhao H, Gao Y, Tang Z (2015) Ultrathin platinum nanowires grown on single-layered nickel hydroxide with high hydrogen evolution activity. Nat Commun 6:6430

Yu X, Manthiram A (2018) Scalable membraneless direct liquid fuel cells based on a catalyst-selective strategy. Energ Environ Mater 1:13–19

Zhang W, Lai W, Cao R (2017a) Energy-related small molecule activation reactions: oxygen reduction and hydrogen and oxygen evolution reactions catalyzed by porphyrin- and corrole-based systems. Chem Rev 117:3717–3797

Zhang T, Li SC, Zhu W, Zhang ZP, Gu J, Zhang YW (2017b) Shape-tunable Pt-Ir alloy nanocatalysts with high performance in oxygen electrode reactions. Nanoscale 9:1154–1165

Zhang R, El-Refaei SM, Russo PA, Pinna N (2018a) Metal phosphonate coordination networks and frameworks as precursors of electrocatalysts for the hydrogen and oxygen evolution reactions. J Nanopart Res 20:146

Zhang P, Li Z, Zhang S, Shao G (2018b) Recent advances in effective reduction of graphene oxide for highly improved performance toward electrochemical energy storage. Energ Environ Mater 1:5–12

Zhao F, Kong W, Hu Z, Liu J, Zhao Y, Zhang B (2016) Tuning the performance of Pt–Ni alloy/reduced graphene oxide catalysts for 4-nitrophenol reduction. RSC Adv 6:79028–79036

Zhu CR, Gao D, Ding J, Chao D, Wang J (2018) TMD-based highly efficient electrocatalysts developed by combined computational and experimental approaches. Chem Soc Rev 47: 4332–4356

Zou X, Liu Y, Li GD, Wu Y, Liu DP, Li W, Li HW, Wang D, Zhang Y, Zou X (2017) Ultrafast formation of amorphous bimetallic hydroxide films on 3D conductive sulfide nanoarrays for large-current-density oxygen evolution electrocatalysis. Adv Mater 29:1700404

Zou X, Wu Y, Liu Y, Liu D, Li W, Gu L, Liu H, Wang P, Sun L, Zhang Y (2018) In situ generation of bifunctional, efficient Fe-based catalysts from mackinawite iron sulfide for water splitting. Chem 4:1139–1152